Journal of Materials Chemistry A

ROYAL SOCIETY OF CHEMISTRY

PAPER

View Article Online
View Journal

Cite this: DOI: 10.1039/d6ta00720a

Polyampholyte graft copolymers as unimolecular matrices for noble metal-free and visible light-driven hydrogen evolution by eosin Y and molybdenum phosphide

Vathsalya T. Sundarraj,[a] Lingli Ni,[b] Marius Hermesdorf,[b] Kilian Pollok,[ce] Mariet Sibi Puthanagady,[fg] Benjamin Dietzek-Ivanšić,[h] Falko Langenhorst,[ce] Martin Oschatz[bcd] and Felix H. Schacher[*acdi]

Light-driven water splitting is a promising way to sustainably produce hydrogen as a renewable energy carrier. For this, immobilization of different catalytically active building blocks within soft and adaptive matrices plays a key role towards the defined preparation of multi-component hybrid materials. Herein, we present a combination of molybdenum phosphide (MoP, catalyst) and eosin Y (EY, photosensitizer), both immobilized within polyampholytic polydehydroalanine-*graft*-*n*-propyl phosphonic acid acrylamide (PDha-*g*-*n*PAA) graft copolymers. Analytical techniques such as nuclear magnetic resonance (NMR) and Raman spectroscopy confirmed successful graft copolymer formation, while X-ray photoelectron spectroscopy (XPS) and transmission electron microscopy (TEM) analyses further confirmed the immobilization of the EY and MoP, as evidenced by characteristic elemental signals and discrete MoP crystallites within the graft copolymer matrix. The catalytic activity for hydrogen evolution was investigated in aqueous triethanolamine (TEOA) solutions under green light irradiation ($\lambda \geq 500$ nm). This resulted in improved hydrogen production (~2.5 $mmol_{H_2}$ h^{-1} g^{-1}) when compared to a system without graft copolymer (~0.9 $mmol_{H_2}$ h^{-1} g^{-1}). The catalytic activity is attributed to the ability of the graft copolymer to stabilize and spatially confine the active units, while simultaneously acting as a bridge to facilitate proton and electron transfer between the EY and MoP.

Received 25th January 2026
Accepted 22nd May 2026

DOI: 10.1039/d6ta00720a

rsc.li/materials-a

Introduction

Studies for a cleaner and more eco-friendly approach to produce energy are important to reduce human's dependency on non-renewable energy resources. One of the most promising alternatives is the large-scale utilization of hydrogen (H_2) as a recyclable energy carrier. It can be used in fuel cells and produces no greenhouse gas emissions when combusted with oxygen, as the only significant product is water vapor.[1] Therefore, researchers are developing a wide range of technologies to produce hydrogen economically and sustainably, primarily *via* water electrolysis but also from other feedstocks such as natural gas and biomass. Among these, light-driven solar water splitting stands out as a promising approach to reduce dependence on fossil fuels by directly harnessing solar energy.[2] Extensive efforts have been made in the search for catalyst materials that work under visible light to efficiently utilize solar energy.[3,4] Recent approaches towards hydrogen evolution are therefore targeting visible-light harvesting through use of photosensitizers,[5] introduction of cocatalysts,[6] band gap engineering,[7] electron relays such as polyoxometalates,[8] or the use of novel semi-conducting materials.[9]

Xanthene dyes, a class of low-cost organic compounds which function as photo-redox catalysts, have proven to be excellent sensitizers for light-driven hydrogen evolution reaction (HER).[10] Eosin Y, a widely used xanthene dye, is employed not only in ternary photosensitization systems composed of dye, semiconductor, and cocatalyst, but also in binary systems composed of dye and cocatalyst.[10] Recently, transition metal phosphides

[a]*Institute of Organic Chemistry and Macromolecular Chemistry (IOMC), Friedrich Schiller University Jena, Lessingstraße 8, 07743 Jena, Germany*
[b]*Institute for Technical Chemistry and Environmental Chemistry, Friedrich Schiller University Jena, Philosophenweg 7a, 07743 Jena, Germany*
[c]*Center for Energy and Environmental Chemistry Jena (CEEC Jena), Friedrich Schiller University Jena, Philosophenweg 7a, 07743 Jena, Germany*
[d]*Helmholtz Institute for Polymers in Energy Applications Jena (HIPOLE Jena), Lessingstraße 12-14, 07743 Jena, Germany*
[e]*Institute of Geosciences, Friedrich Schiller University Jena, Burgweg 11, 07749 Jena, Germany*
[f]*Institute of Physical Chemistry, Friedrich Schiller University Jena, Helmholtzweg 4, 07743 Jena, Germany*
[g]*Leibniz-IPHT, Albert-Einstein-Straße 9, 07745, Jena, Germany*
[h]*Leibniz Institute of Surface Engineering, Permoserstraße 15, 04318 Leipzig, Germany*
[i]*Jena Center for Soft Matter (JCSM), Friedrich Schiller University Jena, Philosophenweg 7, 07743 Jena, Germany. E-mail: felix.schacher@uni-jena.de*

(TMPs) have gained attention as water-splitting catalysts and cocatalysts due to their excellent catalytic properties, long-term stability, and the ability to catalyse both HER and oxygen evolution reactions (OER) in alkaline solutions.[11] Early research focused on Ni- and Co-based phosphides as non-platinum alternatives for hydrogen evolution.[12,13] Recently, molybdenum phosphides (MoP and MoP_2) became highly desirable cocatalysts among TMPs due to their high electronic conductivity and low HER overpotential. These materials have been widely employed as electrocatalysts for HER.[14,15] Dada *et al.* demonstrated that crystallographic facets enhance the catalytic performance of MoP.[16] The metallic conductivity of MoP facilitates the efficient migration of photo-generated carriers,[17,18] and it is also considered an effective 'H delivery' system,[19,20] making it increasingly popular for photocatalytic HER applications. Typically, MoP is synthesized using orthophosphate as the phosphorus source *via* the temperature-programmed reduction (TPR) method at high temperatures (>650 °C) under H_2 or H_2/Ar atmospheres.[21,22] However, an alternative has been reported by Xu *et al.*, utilizing hypophosphite as the phosphorus source and employing a simpler heat treatment process for TMP preparation.[23]

Given that the catalysis often occurs on the surface of catalysts, the improvement of compatibility between catalytic units and water is very critical yet often represents a challenge in heterogeneous catalysis. With respect to multi-component hybrid materials, the immobilization of catalysts, cocatalysts and photosensitizers within polymer matrices plays a key role in integrating the individual components of light-driven catalytic systems. This has been realized on solid substrates such as semiconductors (p-Si),[24] carbon nanomaterials,[25] and metal oxides.[26] Soft matrices based on polyelectrolytes exhibit excellent dispersibility in aqueous environments, providing a stable colloidal scaffold with multiple binding sites for various catalytic materials.[27] Recently, we reported two different polyampholyte graft copolymers, poly(dehydroalanine)-*graft*-(*n*-propyl phosphonic acid acrylamide) (PDha-*g*-*n*PAA) and poly(-dehydroalanine)-*graft*-poly(ethylene glycol) (PDha-*g*-PEG), assisting organic photosensitizers based on EY and perylene monoimides (PMI) in light-driven catalytic hydrogen evolution with $(NH_4)_2[Mo_3S_{13}]$.[27,28] PDha serves as a suitable support with a high density of functional (charged) groups that exhibit strong interactions with metal nanoparticles and dyes in water. Moreover, it contains positively charged amino groups as well as negatively charged carboxylic acid moieties, allowing for the specific interaction with various compounds.[29] Further modification by the introduction of grafted side chains enabled improvements in solubility,[30] efficient dispersion of carbon nanomaterials,[31] and the use as multi-responsive sensors for the detection of metal cations.[32]

Phosphonic acid-bearing polymers have also been reported as potential substrates for applications in tissue engineering and drug delivery.[33,34] Polyacrylamides functionalized with phosphonic acids exhibited improved hydrolytic stability compared to their polyacrylate and polymethacrylamide analogues.[35] Nabiyan *et al.* reported that the attachment of phosphonic acid side chains to a PDha backbone increased solution stability and provided strong anchoring groups on the surface of TiO_2 nanoparticles.[27]

Herein, *n*-propyl phosphonic acid acrylamide (*n*PAA) is used to modify PDha towards tailor-made polyampholyte graft copolymers. These are then used as unimolecular soft matter matrices to improve the stabilization and spatial confinement of both EY and molybdenum phosphide nanocrystals in aqueous media. This overall combination not only enables visible light-driven catalysis but also facilitates the physical integration of materials, which has not been possible before. Although the mere combination of MoP and EY has already been reported, their hydrogen evolution performance is highly dependent on the mode of interaction due to issues like quenching and instability. These challenges have been effectively addressed by immobilization of both components within the polyampholyte graft copolymers.

Experimental section

Chemicals

N-(*tert*-Butoxycarbonyl)-D-serine methyl ester (Boc-Ester, 98%) was purchased from Carbolution Chemicals GmbH, St. Ingbert, Germany. BlocBuilder MA initiator was kindly provided by a co-worker synthesized using the literature procedure.[36] Methanesulfonyl chloride (>99.7%), *n*-propylamine (≥99%), ethanol (95%), ethyl acetate (99.8%), hexane (95%), trifluoroacetic acid (TFA, 99%), trioxane (≥99%), acryloyl chloride(97%), sodium molybdate dihydrate ($Na_2MoO_4 \cdot 2H_2O$, ≥99%), sodium hypophosphite monohydrate ($NaH_2PO_2 \cdot H_2O$, ≥99%), tetrahydrofuran (THF, ≥99.9%), silica gel (for column chromatography), triethylamine (TEA, ≥99.5%), methanol (≥99.9%), hydrochloric acid (HCl, 37%), and bromotrimethylsilane (TMSBr, 97%) were purchased from Sigma-Aldrich, Taufkirchen, Germany. Deuterated solvents such as deuterium oxide (D_2O), sodium deuteroxide 30% in D_2O (NaOD), chloroform-d ($CDCl_3$) were purchased from Deutero GmbH, Kastellaun, Germany. Sodium sulphate (Na_2SO_4, 99%) was purchased from Grüssing GmbH, Filsum, Germany. Dichloromethane (DCM, ≥99.9%) was purchased from VWR Chemicals, Dresden, Germany. Diethyl vinyl phosphonate (97%) was purchased from Fisher Scientific, Schwerte, Germany. 1,4 dioxane (≥99.5%), potassium bisulphate ($KHSO_4$, ≥99.9%), sodium hydroxide (NaOH, ≥98%), potassium hydroxide (KOH, ≥85%) were purchased from Carl ROTH, Karlsruhe, Germany.

Nuclear magnetic resonance (NMR) spectroscopy

^{1}H NMR spectra were performed on a Bruker AC 300 MHz using $CDCl_3$, MeOD and D_2O/NaOD as solvents at a temperature of 298 K. The spectra were referenced by using the residual signal of the deuterated solvent.

Dynamic light scattering (DLS)

DLS measurements were performed using an ALV laser CGS3 Goniometer equipped with a 633 nm HeNe laser (ALV GmbH, Langen, Germany) at 25 °C. Detection angle of 90° was used.

The CONTIN analysis of the obtained correlation functions was performed using the ALV 7002 FAST Correlator Software.

Zeta potential

The measurements of the photocatalytic system were performed using a Malvern Zetasizer Nano ZS equipped with a 633 nm He–Ne laser. All measurements were conducted in the native state at 22 °C without further pH adjustment, resulting in a measured pH of approximately 9. The electrophoretic mobility was determined using the M3-PALS technique at a detection angle of 13°, and the zeta potential was calculated using the Smoluchowski approximation. Each reported value represents the average of three independent runs. For each sample, measurements were taken after an equilibration time of 120 seconds.

Size exclusion chromatography (SEC)

SEC measurements using $CHCl_3$ as the eluent with flow rate of 1 mL min^{-1} was performed using an Agilent 1260 Infinity system equipped with a 1260 ALS (G1310B) autosampler, 1260 IsoPump (G1310B) and three consecutive PSS SDV, 5 μm, 8 × 300 mm columns with polystyrene calibration. The column oven was set to 30 °C, and signals were detected using a 1260 RID (G1315D) and a 1260 DAD VL (G1329B) detector.

SEC measurements in DMSO were performed on a Jasco instrument using DMSO with 0.5% LiBr as the solvent at a flow rate of 0.5 mL min^{-1} at 65 °C. Pullulan was used for calibration. The system was equipped with PSS NOVEMA 3000 °A/300 °A columns, PU-980 pump, and a RI-930 detector.

Thermogravimetric analysis (TGA)

TGA measurements were carried out under synthetic air flow in a PerkinElmer TGA800 device by heating from 30 °C to 1200 °C with a heating rate of 20 °C min^{-1}.

Transmission electron microscopy (TEM)

TEM images and selected area electron diffraction (SAED) patterns were acquired with a 200 kV FEI Tecnai G2 FEG equipped with a 2k Gatan CCD camera. Chemical compositions were determined by aid of an X-Max^n 80 T SDD Oxford energy-dispersive X-ray (EDX) system. Samples were prepared by the deposition of 10 μL of the sample solution onto Quantifoil carbon support films using a Cu-400 support mesh for dry TEM and 2/2 holey carbon films on the same mesh for Cryo-Transmission Electron Microscopy (Cryo-TEM). Cryo-TEM samples were blotted and frozen by plunging into freezing liquid ethane using a Vitrobot Mark IV before being stored under liquid nitrogen and transferred to the microscope using a Gatan transfer stage. Micrographs were evaluated using the software ImageJ.

X-ray photoelectron spectroscopy (XPS)

For XPS analysis the powder samples were pressed onto the sample holder using adhesive Cu-foil. The samples were then analyzed using the K-alpha spectrometer from Thermo Fisher. The measurement was performed in ultra-high vacuum conditions. A flood gun, calibrated to C=C in PE 284.8 eV ± 0.1 eV, was employed for charge compensation. The recorded spot size was 400 μm. For compositional data, survey spectra were recorded with a step size of 1 eV and a pass energy of 100 eV. High-resolution C 1s, O 1s, Mo 3d, P 2p and Br 3d spectra were obtained with a step size of 0.05 eV and a pass energy of 30 eV, with 5 scans for each sample. All spectra were analyzed using Avantage v6.6.0 software from Thermo Fisher Scientific.

Ultrasonication

Ultrasonification was carried out using a Sonic VibraCellVC505 500 watt Ultrasonic processor. To reduce noise, a sound abating enclosure was used.

Powder X-ray diffraction

X-ray diffraction (XRD) was recorded on a Bruker D8 Advance X-ray diffractometer (Germany) operating with Cu Kα radiation. The measurement was carried out at an operating voltage of 40 kV and 40 mA. The diffraction pattern was collected over a 2θ range of 20° to 80° with a step size of 0.01° and a dwell time of 30 seconds per increment.

Phase quantification was conducted *via* Rietveld refinement using Profex 5 software with BGMN engine. Structural models for MoP and MoP_2 were based on the crystal structures reported by Rundqvist and Lundström (1963).[37] To accurately model the complex background and non-crystalline components, two broad amorphous peaks centered at peaks 23° and 36° (2θ) were included in the refinement strategy.

Fourier-transform infrared spectroscopy (FT-IR)

FTIR spectra were recorded on a PerkinElmer Frontier spectrometer equipped with a Specac Golden Gate ATR accessory featuring a high-temperature diamond top plate and an integrated temperature controller. Spectra were collected in the range of 400–4000 cm^{-1}.

Fourier-transform Raman spectroscopy (FT-Raman)

FT-Raman spectra were acquired using a Bruker MultiRam Fourier-transform Raman spectrometer (Bruker Corporation, USA) equipped with a Nd:YAG laser (1064 nm, Klastech DeniCAFC-LC-3/40). Measurements were performed in the range of 0–4000 cm^{-1} at a spectral resolution of 4 cm^{-1}. An incident laser power of 500 mW was used, with 500 scans averaged per acquisition. Data were processed using background correction and vector normalization to ensure comparability.

Nitrogen physisorption

Specific surface areas and porosity were characterized using a Quadrasorb SI apparatus (Quantachrome Instruments) at 77 K. Prior to measurement, samples were outgassed at 398 K under vacuum overnight. The specific surface area of MoP was calculated using the multi-point Brunauer–Emmett–Teller (BET) method ($p/p_0 = 0.05$–0.30), yielding a value of 24 m^2 g^{-1}.

Time-resolved emission measurement

For lifetime measurements, a Hamamatsu streak camera scope C4334 (Hamamatsu Photonics, Japan) was used with a streak time window of ~2 ns. The laser source was a Ti-sapphire laser (Spectra physics Tsunami HP, pumped by a Verdi V10, Coherent laser) that delivered 200-fs pulses centered at 800 nm with a repetition rate of 76 MHz and an average output power of 1.4 W. This train of pulses was used to pump an optical parametric oscillator (OPO) (APE), which generated a train of pulses centered at 505 nm, which were attenuated to a power of <20 mW and used for exciting the sample. Two quartz glass lenses with a 2-inch diameter and a 150 mm focal length were used to collect emission. The instrument response function was measured using SiO_2 nanoparticles and was found to be around 40 ps. A Princeton Instruments Acton SP2300 imaging spectrograph is used to filter specific wavelength ranges, which are then measured by the attached Hamamatsu streak camera.

All samples were prepared in a glovebox and measured in a 1 cm quartz inert cuvette with DI water as the solvent. The measurement was performed in photon-counting mode (MCP gain 17, time range 5) with the emission central wavelength set to 535 nm. All data were processed and fitted using OriginLab 2024b software.

Steady-state measurements

All samples were prepared in a glovebox and measured in a 1 cm quartz cuvette. UV-vis absorption spectra were measured in the range between 400 and 800 nm using a Jasco V-780 UV/vis/NIR spectrophotometer in transmission mode. Baseline correction was done in air, and samples were measured with DI water as reference. Emission measurements were done using an EdInst FLS980 spectrofluorometer at an excitation wavelength of 480 nm.

A detailed description of the synthesis procedures, photocatalytic hydrogen evolution with characterization data can be found in the SI.

Results and discussion

Synthesis and characterisation of PDha-*g*-*n*PAA

High-grafting density of various side chains onto polydehydroalanine has been previously reported.[29–31] In this work, phosphonic acids were selected as the grafting agent, as it was anticipated that a strong interaction with MoP would allow an efficient immobilization within the graft copolymer matrix. The synthesis began with the monomer, *tert*-butoxycarbonylaminomethylacrylate (*t*BAMA), followed by nitroxide-mediated polymerization using alkoxyamine initiator *N*-(2-methylpropyl)-*N*-(1-diethylphosphono-2,2-dimethylpropyl)-*O*-(2-carboxylprop-2-yl) hydroxylamine (BlocBuilder MA) to form poly(*tert*-butoxycarbonylaminomethylacrylate) (P*t*BAMA). TFA/H_2O-mediated deprotection of P*t*BAMA resulted in complete Boc removal (100%) and partial methyl ester hydrolysis (~94%), yielding the statistical copolymer polydehydroalanine-*stat*-poly(aminomethyl acrylate) (PDha-*stat*-PAMA) as the reactive polymeric backbone. *N*-propyl phosphonic acid acrylamide (*n*PAA) was obtained by complete deprotection of the ethyl groups from the phosphonic acids (*n*-propyl-*n*-(2-(diethoxy phosphoryl)ethyl) acrylamide (*n*PEA)) using bromotrimethylsilane and was successfully grafted onto PAMA *via* an aza-Michael addition (Scheme 1). During the grafting process, the pH was maintained at 13, completing hydrolysis of residual methyl esters to carboxylic acids *via* saponification and promoting concurrent conversion of PAMA to polydehydroalanine (PDha, Scheme 2). The resulting graft copolymer exhibited a lower number average molecular weight with $M_n = 13\,500$ and dispersity $Đ = 1.6$ (Fig. S1). Table 1 presents the number average molecular weight, degree of polymerization (DP), and degree of functionalization (DoF), all calculated from NMR and SEC data.

The ^{1}H NMR spectra of *n*PAA indicate that the protecting groups (ethyl ester) have been successfully removed (Fig. S2). In the ^{1}H NMR spectra of PAMA and PDha-*g*-*n*PAA, the polymer backbone peak is clearly visible (~2.3 ppm), and the rest of the peaks from PDha-*g*-*n*PAA can be assigned to the grafting agent (Fig. S3). Therefore, the DoF was found to be 0.37 when using 2 equivalents of grafting agent. In addition, Raman spectroscopy further confirms the presence of *n*PAA in the graft copolymer (Fig. S4a). Additionally, ^{31}P NMR spectrum of the graft copolymer exhibits a distinct peak that corresponds to phosphonic acid groups around 16–18 ppm, further confirming the successful grafting of *n*PAA (Fig. S4b). While higher DoFs are possible when using larger amounts of grafting agent (5, 8 and 9 equivalents), preliminary synthetic trials resulted in graft copolymers with poor aqueous solubility, presumably due to intramolecular complexation taking place. Therefore, a DoF of 0.37 has been selected for this study.

Synthesis and characterisation of molybdenum phosphide (MoP)

The synthesis of MoP was adapted from the procedure reported by Xu *et al.*[23] and involved grinding sodium molybdate dihydrate and sodium hypophosphite monohydrate in an agate mortar, followed by calcination at 400 °C in a nitrogen atmosphere. The resulting product was washed, acid-etched, dried, and collected as a powder. The crystallinity and morphology of the synthesized material are confirmed by XRD and high-resolution transmission electron microscopy (HRTEM) (Fig. 1). The X-ray and electron diffraction data are in line with the structure of hexagonal MoP in space group $P\bar{6}m2$ reported by Rundqvist and Lundström[37] (Fig. 1a). The XRD pattern was refined by the Rietveld method, confirming hexagonal MoP (>95 wt%) as the major phase with excellent fit statistics

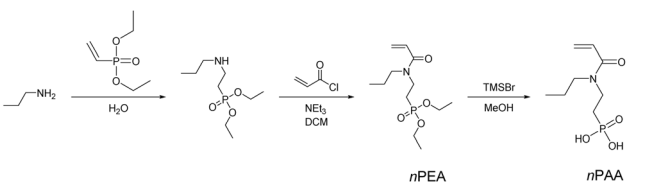

Scheme 1 Synthesis of the grafting agent (*n*PAA).

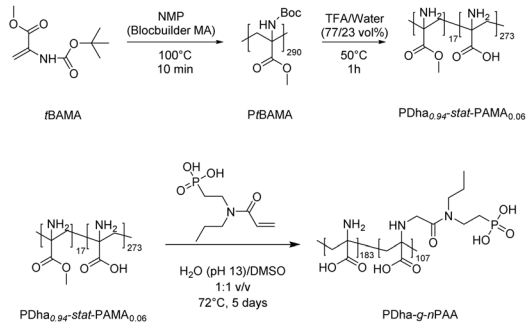

Scheme 2 PtBAMA synthesis by NMP polymerization, PDha-*stat*-PAMA (PDha$_{0.94}$-*stat*-PAMA$_{0.06}$ from ^{1}H NMR, Fig. S3) by TFA/H_2O deprotection, and PDha-*g*-*n*PAA by aza-Michael addition (pH 13).

Table 1 Molecular characteristics of synthesized PtBAMA, PAMA, and PDha-*g*-*n*PAA determined by SEC and NMR. M_n: number-average molecular weight; DP: degree of polymerization; DoF: degree of functionalization. PtBAMA and PAMA for SEC were analyzed in $CHCl_3$ using polystyrene calibration; PDha-*g*-*n*PAA was analyzed in DMSO using pullulan calibration

Sample	M_n, DP, DoF	Dispersity
PtBAMA	69 400 (DP = 290)	1.6
PAMA	29 000	2.1
PDha-*g*-*n*PAA	13 500 (DoF = 0.37)	1.6

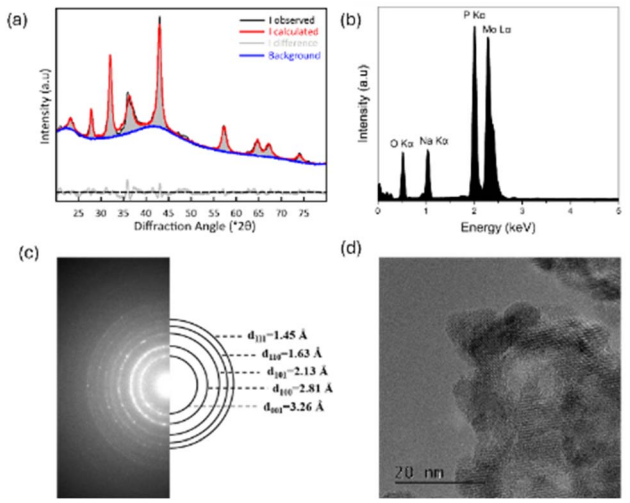

Fig. 1 (a) Powder X-ray diffraction and Rietveld refinement (R_{wp} = 4.62%, χ^2 = 1.46) (b) TEM-EDX spectra of MoP (c) SAED pattern of MoP (left) and indexed overlay (right) showing concentric diffraction rings corresponding to the characteristic *d*-spacings and hkl planes of hexagonal MoP and (d) HRTEM image of nanocrystalline MoP.

(weighted profile *R*-factor R_{wp} = 4.62% and goodness-of-fit χ^2 = 1.46) and yielding an anisotropic crystallite size of approximately 30 nm (27–31 nm depending on direction). Trace MoP_2 (~4.5 wt%) accounts for the additional minor peaks observed. This P-rich impurity arises from the synthesis conditions and does not significantly impact catalytic performance, as MoP_2 exhibits comparable HER activity to MoP due to similar phosphide electronic properties.[38,39] Energy-dispersive X-ray spectroscopy (EDX) analysis further suggests a slight deviation from the stoichiometric molybdenum-to-phosphorus ratio of 1 : 1, with elemental compositions of 48 at% molybdenum and 52 at% phosphorus (Fig. 1b). Additional signals from O and Na are observed, which can be originating from the precursors. XPS confirms the presence of Mo and P at the surface and also shows a C 1s contribution of ~15 at%, arising from ubiquitous adventitious hydrocarbons. This surface carbon contamination is typical for air-exposed in-organic powders and does not affect the bulk Mo:P stoichiometry determined by EDX. (Table S1 and Fig. S6a). The SAED pattern exhibits well-defined concentric rings that can be indexed to the characteristic lattice spacings of hexagonal MoP, confirming its crystalline nature (Fig. 1c). HRTEM images further reveal distinct lattice fringes with crystalline domains up to 20 nm (Fig. 1d). This is reasonably consistent with the XRD-derived crystallite size, noting that XRD provides an ensemble-averaged value whereas HRTEM visualizes individual domains. These results collectively verify the crystalline structure and nanoscale morphology of the synthesized MoP. Furthermore, the textural properties of the MoP were characterized by N_2 physisorption. The material exhibited a specific surface area of 24 m^2 g^{-1}. Assuming an equivalent spherical geometry and a theoretical density of 7.12 g cm^{-3},[37] this corresponds to a particle radius of approximately 17.6 nm. The reasonable agreement between the XRD and N_2 physisorption data (27–31 *vs.* 17.6 nm) confirms that the material exists as discrete crystalline units, supporting the structural model used for subsequent stoichiometric calculations.

Preparation and characterisation of hybrid dispersions

To evaluate the thermal stability of the photocatalytic components, three representative colloidal systems were prepared and analysed by TGA under oxidative conditions (Fig. 2a). In all cases, the concentration of EY was fixed at 0.1 g L^{-1}. Two systems contained PDha-*g*-*n*PAA and EY, prepared with polymer concentrations of 0.5 g L^{-1} and 2 g L^{-1}, respectively, while the

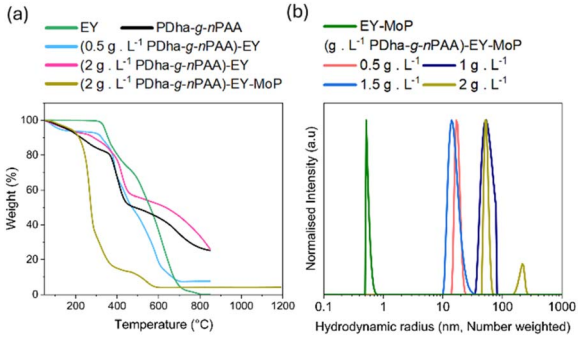

Fig. 2 (a) Thermograms of EY, PDha-*g*-*n*PAA, (PDha-*g*-*n*PAA)-EY with varying ratios of graft copolymer (b) hydrodynamic size distributions of the photocatalytic systems – number weighted DLS plots for EY-MoP and EY-MoP-graft copolymer composites at varying graft copolymer concentrations (0.5, 1, 1.5, and 2 g L^{-1}).

third system comprised the complete photocatalytic formulation (PDha-*g*-*n*PAA, 2 g L^{-1}; EY, 0.1 g L^{-1}; MoP, 0.06 g L^{-1}). Each mixture was dispersed in water, homogenized by ultrasonication, purified by dialysis (MWCO 3.5 kDa), freeze-dried prior to TGA. For comparison, TGA profiles of EY and PDha-*g*-*n*PAA alone were also recorded alongside the three colloidal systems.

The TGA profile of PDha-*g*-*n*PAA showed an initial weight loss up to ~380 °C due to evaporation of bound and residual water. Polymer decomposition commenced thereafter, with the main breakdown occurring between 400–500 °C and leaving ~28% char at 850 °C. Pure EY degraded between 350–800 °C and was fully decomposed without any residual mass. The graft copolymer/EY mixtures exhibited concentration-dependent behaviour: at low graft copolymer loading (0.5 g L^{-1}), the thermal response resembled that of EY, indicating limited influence of the graft copolymer on EY's degradation. At higher loading (2 g L^{-1}), the profile became more similar to PDha-*g*-*n*PAA, with a more gradual weight loss and comparable residual mass. This shift likely results from the increasing dominance of the polymer matrix in the thermal behaviour as its relative mass increases. The similar final residues of pure PDha-*g*-*n*PAA and the 2 g L^{-1} copolymer/EY sample likely arise from the complete decomposition of EY and differences in residual water content after drying.

To understand the influence of the catalyst on the final hybrid material, the thermal behavior of pure MoP was first considered (Fig. S5). Upon initiation of the TGA measurement at 30 °C, an initial mass loss of approximately 5% is observed up to 280 °C. This is attributed to the desorption of physisorbed water and atmospheric gases from the MoP surface rather than material decomposition. Subsequently, MoP exhibits a distinct increase in sample weight during thermogravimetric analysis under synthetic air. This weight gain initiates around 400 °C and continues until approximately 800 °C, ultimately reaching an increase of nearly 15%. This process is attributed to the progressive oxidation of MoP, most likely forming molybdenum oxides such as MoO_3. Since no significant MoO_2 peaks are observed in the XRD analysis, the direct oxidation of MoP to molybdenum trioxide is presumed to drive the majority of the observed weight increase, rather than oxidation of MoO_2. The sample began to lose weight around 825 °C, likely due to sublimation of MoO_3, which has a melting point of 801 °C and starts to decompose and sublime between 780–1200 °C.[40] Notably, the colloidal system (PDha-*g*-*n*PAA-EY-MoP) displayed a distinct degradation pattern. The introduction of MoP into the system lowered the thermal stability among all tested samples. A sharp weight loss was observed between 200–400 °C, followed by a second phase of weight loss up to ~600 °C. This was accompanied by a small weight gain (bump) during this intermediate range and a plateau extending up to 1200 °C. The initial steep degradation may be attributed to enhanced chain scission catalyzed by MoP. The immobilisation of MoP nanoparticles introduces catalytic sites that lower the activation energy for degradation and accelerate mass loss by increasing the rate of volatile product formation (*e.g.*, CO_2, H_2O, or fragmented monomers).[41,42] The weight gain around 400 °C is consistent with the oxidative formation of molybdenum oxides, indicating MoP's active participation in thermal reactions.[40] These findings suggest that, even though addition of MoP results in a less stable system from a purely thermal perspective, the altered degradation profile originates from the close interfacial contact and high local concentration of the active components. This strong physical and electronic coupling likely allows the MoP nanoparticles to lower the activation energy for the thermal decomposition of the polymer matrix at elevated temperatures (>200 °C). However, since photocatalytic water splitting is conducted in aqueous media at ambient temperatures (<50 °C), this localized catalytic effect does not impact the operational stability of the material. Instead, the observed reduction in the TGA decomposition onset serves as indirect evidence of the efficient integration of the catalyst within the graft copolymer scaffold, which is essential for driving charge separation and hydrogen evolution under ambient conditions.

Based on the grafting density obtained from NMR (≈290 repeat units and ≈107 grafted units per PDha-*g*-*n*PAA chain) and the equivalent spherical radius (~17.6 nm) derived from gas sorption data, the stoichiometry of the photocatalytic formulation corresponds to approximately 4.2×10^4 graft copolymer chains per MoP nanoparticle in 1.5 g L^{-1} dispersion of graft copolymer sample. This high graft copolymer-to-MoP particle ratio indicates that the photocatalytic system operates with a significant excess of graft copolymer. While steric constraints likely prevent the simultaneous physical adsorption of all chains onto the MoP surface, this ratio ensures that each catalytic center can be embedded within graft copolymer-rich environment. This matrix serves to spatially confine the active units and facilitates the efficient transport of protons and electrons; the high local concentration of phosphonic acid and amide groups creates a continuous hydrogen-bonding network that acts as a proton relay, while the hydrated nature of the dispersed polyampholyte matrix maintains sufficient molecular mobility for the EY photosensitizer to remain in close electronic proximity to the MoP surface. Fig. 3 combines a schematic representation with a TEM micrograph (Fig. 3b), in which the darker regions correspond to electron-dense MoP-rich domains embedded in a lighter graft copolymer-containing matrix. This confirms the presence of MoP within graft copolymer-based colloidal assemblies, although the local distribution is likely inhomogeneous and may be affected by drying and precipitation during TEM sample preparation. In aqueous media, EY remains molecularly dissolved and therefore is not visible in TEM; its co-localisation with the graft copolymer and MoP is therefore depicted schematically (Fig. 3a). To gain deeper insights into the morphology without drying artifacts, cryo-TEM was performed across the relevant polymer concentrations and 1 g L^{-1} is shown here (Fig. 3c). This technique was specifically chosen to preserve the native hydration state of the graft copolymer and to eliminate potential artifacts arising from drying-induced aggregation. The image shows spherical graft copolymer assemblies with regions of enhanced contrast, indicating the presence of electron-dense inorganic material within the graft-copolymer matrix. However, individual MoP crystallites are not directly resolved in the micrograph, likely

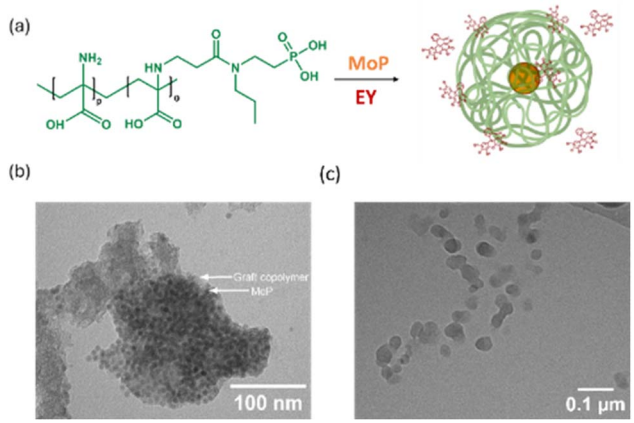

Fig. 3 (a) Chemical structure of the graft copolymer PDha-*g*-*n*PAA with schematic representation of the functionalised copolymer after incorporation of EY and MoP nanocrystals *via* sonication illustrating a spherical MoP particle embedded within a coiled polymer network. (b) TEM image highlighting local MoP distribution within the graft copolymer-based colloidal assemblies. (c) Cryo-TEM image of PDha-*g*-*n*PAA-EY-MoP vitrified at a graft copolymer concentration of 1 g L^{-1}.

because of the combined effects of sample thickness, and embedding within the hydrated graft copolymer domain.

To further confirm the formation of colloidal hybrids, DLS measurements were performed, while zeta potential measurements were conducted to evaluate the colloidal stability of the system. The samples for these experiments were prepared as follows: EY (0.1 g L^{-1}) and MoP (0.06 g L^{-1}) were dispersed in water and ultrasonicated using a finger-tip probe for 5 minutes. Different concentrations of graft copolymer (0.5, 1, 1.5, 2 g L^{-1}) was then added to 2.5 mL of this EY-MoP solution, followed by further ultrasonication. Finally, 10 v/v% triethanolamine (TEOA) was introduced (pH = 9) before measurements were conducted.

The number-weighted DLS profile of the EY-MoP reference dispersion (without graft copolymer) shows a narrow distribution below 1 nm (Fig. 2b). This signal is attributed to the molecularly dissolved EY and potentially sub-nanometer MoP species present in the dispersion. While HRTEM reveals discrete MoP crystallites up to ~20 nm, their relatively lower number density in the reference dispersion compared to the high molar concentration of EY results in the dominance of the EY molecular species in the number-weighted distribution. Upon addition of PDha-*g*-*n*PAA, the hydrodynamic radius increases systematically with copolymer concentration. At 0.5 g L^{-1}, a single, relatively narrow population centred at ~20 nm is observed, consistent with well-dispersed graft copolymer/MoP assemblies. This hydrodynamic radius is reasonably consistent with the Scherrer size derived from XRD (17.7 nm). Such concordance between the crystallographic and hydrodynamic radii indicates that, at low concentrations, the graft copolymer effectively stabilizes individual MoP nanoparticles as discrete units, providing a thin hydrated shell that suppresses the formation of larger aggregates. Increasing the copolymer concentration to 1 and 1.5 g L^{-1} leads to peak broadening and a shift towards larger sizes (~30–60 nm), indicative of partial secondary aggregation or cluster formation. At 2 g L^{-1}, a bimodal distribution emerges with populations around ~50 and ~200 nm, suggesting the formation of larger graft copolymer-rich aggregates. These data support that the graft copolymer provides effective steric stabilization and suppresses MoP aggregation at low to intermediate concentrations, whereas excessive copolymer content promotes secondary association into larger assemblies (>100 nm), which is expected to reduce the fraction of optimally nano-confined, catalytically accessible domains. Taken together with the gas sorption results, these DLS data support a model in which a specific subset of the graft copolymer chains directly stabilizes the MoP nanocrystals. At higher loadings, the excess chains likely undergo intermolecular association, contributing to the formation of larger, polymer-rich aggregates rather than further surface functionalization.

Zeta potential measurements further supported these findings, showing that colloidal stability was highest at an optimum graft copolymer concentration (1 g L^{-1}), beyond which a reduction in zeta potential magnitude was observed. The initial zeta potential of the graft copolymer-free system was measured at −27.5 mV, primarily due to the deprotonated carboxylate ($-COO^-$) and phenolate ($-O^-$) groups of EY, along with the presence of TEOA under alkaline conditions (pH 9), indicating a moderately stable, negatively charged dispersion. With the gradual addition of graft copolymer, the zeta potential magnitude increased, reaching a maximum value of −30.6 mV at 1 g L^{-1} polymer, suggesting improved electrostatic stabilization. This indicates that negatively charged carboxylic acid and phosphonic acid groups of the graft copolymer contribute to the electrostatic repulsion and thereby an improved colloidal stability. However, beyond this concentration, the magnitude of zeta potential decreased, indicating potential graft copolymer-induced aggregation.

To elucidate the interactions and immobilization of MoP and EY within the PDha-*g*-*n*PAA matrix, XPS analysis was performed for the C 1s, O 1s, Mo 3d, and P 2p regions (Fig. 4). The C 1s spectrum (280–290 eV) displays a series of peaks within the range expected for the polymer backbone, phosphonic acid side chains, amide environments, and dye-derived functionalities (Fig. 4a). These features may correspond to aliphatic C–C, aromatic or heteroatomic C–N and C–P linkages, various carbonyl environments, and highly oxidized or conjugated carbon, according to the chemical composition of the system.[27] Similarly, The O 1s spectrum (529–535 eV) shows several components attributable to oxygen in carbonyl, phosphonate/phosphate, molybdenum oxide, and ester/hydroxyl environments as anticipated from the composition of the (PDha-*g*-*n*PAA)-EY-MoP system (Fig. 4b). Signals for potassium are also present, consistent with residual K^+ from the grafting procedure.

The Mo 3d spectrum displays well-defined doublets at 228.1/231.3 eV (Mo–P, molybdenum phosphide), as well as peaks at ~229.4/232.5 eV and ~232.6/235.7 eV, which can be assigned to Mo^{4+}–O (MoO_2) and Mo^{6+}–O (MoO_3) species from partial surface oxidation, respectively (Fig. 4c). The P 2p region shows

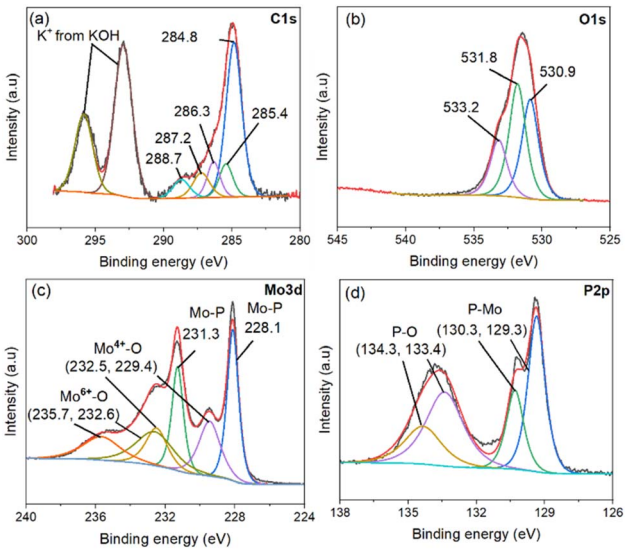

Fig. 4 XPS spectra of C 1s (a), O 1s (b), Mo 3d (c) and P 2p (d) of hybrid system (PDha-*g*-*n*PAA)-EY-MoP.

a doublet at ~129.3/130.3 eV (P–Mo, molybdenum phosphide), and additional peaks at 133.4 and 134.3 eV, attributable to phosphorus in phosphonate and phosphate environments (Fig. 4d).[23] The combined observation of Mo–P and P–Mo features, together with O 1s and C 1s peaks consistent with the chemical structure of the copolymer and incorporated species, supports the successful immobilization of MoP nanoparticles within the phosphonic-acid-functionalized network. Bromine is detected only in trace quantities and is therefore reported qualitatively from the survey spectra shown in Fig. S6. The corresponding survey spectra and quantified atomic percentages for the graft copolymer, (Pdha-*g*-*n*PAA)-EY and (PDha-*g*-*n*PAA)-EY-MoP are summarized in Fig. S6(b–d) and Table S1. Fig. S7 confirms the successful incorporation of brominated EY into the PDha-*g*-*n*PAA, with characteristic Br 3d signals and shifted C 1s peaks validating the hybrid structure. The graft copolymer alone shows high C 1s and O 1s amounts, as expected for the PDha and *n*PAA units. Upon addition of EY and, more strongly, MoP, the relative C 1s intensity decreases while Br 3d, Mo 3d and P 2p contributions emerge and N 1s slightly increases, reflecting the incorporation of the brominated dye and the inorganic MoP phase and a corresponding reduction of the purely organic surface fraction. The elevated P 2p atomic percentage in the hybrid relative to the bare polymer is consistent with the combined presence of grafted phosphonate groups and surface-exposed phosphorus from MoP. A weak Si 2p signal is observed in some XPS spectra and is attributed to trace silicon-containing contamination, most likely from the substrate or laboratory environment, rather than from the MoP, EY or graft-copolymer components. Therefore, in the full hybrid (PDha-*g*-*n*PAA)-EY-MoP, the simultaneous presence of Mo 3d, P 2p, Br 3d, C 1s, O 1s, and N 1s signals demonstrates that MoP, EY, and the graft copolymer are all present within the XPS sampling depth of the material surface.

Light-driven hydrogen evolution

The light-driven hydrogen evolution experiments were conducted at ambient temperature and under atmospheric pressure conditions. A visible-light LED source ($\lambda = 530 \pm 50$ nm) was employed for irradiation, delivering an incident photon flux of 0.302 μmol s^{-1} at an operating current of 330 mA. The experiments were carried out in a custom-built, air-cooled photoreactor equipped with a sample holder accommodating eight vials positioned 5 cm above the light source.[43] The amount of hydrogen was determined through gas chromatography. Hydrogen evolution rates are expressed as $mmol_{H_2}\ h^{-1}\ g_{MoP}{}^{-1}$. Reactions were conducted for 3 h with 10 vol% TEOA as sacrificial agent. In Fig. 5a, a constant MoP loading of 100 mg L^{-1} was used while varying the graft copolymer concentration (0.5, 1.0, 2.0 g L^{-1}). In Fig. 5b, a constant copolymer concentration of 2.0 g L^{-1} was maintained while varying the MoP loading (5, 15, 60, 100 mg L^{-1}). Data represent mean values from replicate experiments. The increase in H_2 production with higher copolymer content (Fig. 5a) is attributed to effective stabilization of the catalyst in solution, which prevents MoP nanoparticle aggregation. In addition, the introduction of graft copolymer possibly improves the interface between the catalytic units and the aqueous medium, EY, and MoP within the immobilized polymer matrix. The immobilization of EY within the PDha-*g*-*n*PAA matrix is primarily driven by electrostatic attraction between the dianionic dye species (active form at pH > 3.8) and the polyampholytic backbone. Additionally, the high density of phosphonic acid and acrylamide functional groups provides a network of hydrogen-bonding sites that further stabilize the dye molecules within the hydrated polymer shell. While covalent immobilization strategies offer permanent dye attachment, they can often restrict the conformational freedom required for optimal electronic interaction between the photosensitizer and the catalyst surface.[44,45] In contrast, our non-covalent approach utilizes conformational flexibility of the hydrated graft copolymer matrix to maintain EY in close proximity to the MoP centers while allowing sufficient molecular mobility for efficient electron transfer.[27,46] This 'dynamic' proximity mimics the benefits of covalent linking (high local concentration) without the synthetic complexity or potential loss of dye activity associated with rigid chemical spacers which can restrict the optimal electronic alignment between the

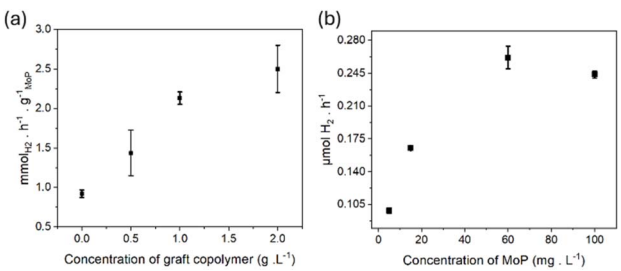

Fig. 5 (a) H_2 evolution rate per gram of MoP used based on the concentration of graft copolymer and (b) H_2 evolution rate used based on the concentration of MoP in aqueous solution.

photosensitizer and the catalyst surface.[47] As discussed in the following section, this hypothesized dynamic interaction and local confinement are directly corroborated by time-resolved fluorescence studies.

As discussed in the TEM section, sorption-based estimations based on the BET model place the system in a pronounced graft copolymer-excess regime. Nevertheless, the presence of a large reservoir of chains around each MoP nanocrystal is expected to increase the local density of EY and grafting sites in its vicinity, thereby facilitating energy and electron transfer from excited EY to MoP and enhancing hydrogen evolution.[23] In contrast to a homogeneous system with free MoP, where nanoparticles tend to sediment and lose interparticle contact with EY, the graft-copolymer matrix provides a dynamically stabilized, well-dispersed environment that sustains continuous electron transfer. At higher polymer loadings the hydrogen-production rate approaches a plateau, which can reasonably be attributed to increasing solution viscosity and growing graft copolymer-rich aggregates that begin to hinder diffusion and limit further gains in catalytic performance.

In case of varying MoP concentrations, the amount of hydrogen is reported by moles of hydrogen produced per time of photoreaction. It is evident that the hydrogen production increases until 0.06 g L^{-1} concentration of MoP and then shows a downward path (Fig. 5b). This might be due to the fact that a sufficient amount of MoP particles were immobilized within the polymer matrix and reached its optimum (0.06 g L^{-1}). At higher MoP concentrations, more scattering of incident light could be the reason due to the free MoP particles in solution, which in turn reduces the amount of light that reaches the photosensitizer sites. This decrease in light intensity lowers the energy available for the light-driven catalytic reaction, thereby leading to a reduction in hydrogen production efficiency. Also, at higher concentrations, MoP could aggregate or form clusters, which reduces the active surface area available for the catalytic reaction.

Moreover, the reproducibility of the experiments was investigated, where the standard deviation is measured to be in the range of 0.05–0.3 $mmol_{H_2}\ h^{-1}\ g_{MoP}{}^{-1}$ in Fig. 5a and 0.003–0.004 $\mu mol_{H_2}\ h^{-1}$ in Fig. 5b. The photocatalytic system demonstrated sustained hydrogen evolution over a period of 150 h, with continuous gas production observed throughout the experiment. The maximum cumulative hydrogen yield reached 63.74 $mmol_{H_2}\ h^{-1}\ g_{MoP}{}^{-1}$ with 1 g L^{-1} of graft copolymer in comparison to the system without graft copolymer (26.91 $mmol_{H_2}\ h^{-1}\ g_{MoP}{}^{-1}$), confirming the long-term activity of the immobilised graft copolymer system. To probe photosensitizer–polymer interactions and excited-state dynamics under conditions mimicking catalysis, steady-state and time-resolved fluorescence spectroscopy were performed (Fig. 6). Graft copolymer concentrations (0.5, 1.0, 1.5, 2.0 g L^{-1}) matched those in H_2 evolution experiments, while EY and MoP loadings were significantly reduced for spectroscopy (EY: 0.001 g L^{-1}, MoP: 0.0006 g L^{-1}) compared to catalytic runs (EY: 0.1 g L^{-1}, MoP: 0.06 g L^{-1}). This reduction in loading was strictly necessary to maintain an optical density below 0.15 at the excitation wavelength of 480 nm, thereby eliminating artifacts from inner-filter

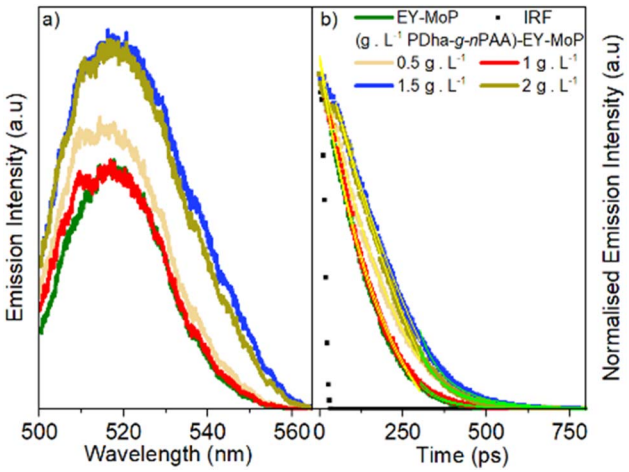

Fig. 6 (a) Emission spectra of EY in the presence of MoP and TEOA with increasing concentrations of PDha-*g*-*n*PAA (0 to 2 g L^{-1}), showing an enhancement in emission intensity. (b) Time-resolved fluorescence decay kinetics of the same systems. The black dot represents the instrument response function (IRF). Solid lines represent the segmented fit using an exponential function for the early-phase (t < 300 ps) and a power-law function for the late-phase (300 ps < t < 1200 ps) dynamics. All measurements were performed at reduced EY (0.001 g L^{-1}) and MoP (0.0006 g L^{-1}) loadings to minimize inner-filter effects.

effects, reabsorption, and non-specific self-quenching that would otherwise obscure the intrinsic interaction kinetics. Fig. 6a shows steady-state emission spectra and time-resolved decay kinetics of EY at these polymer concentrations with MoP and TEOA. The emission intensity increases non-linearly with added polymer concentration compared to the polymer-free system, while the fast decay time constants from the early phase fit (Table S2) also increase. This rise in excited-state lifetime indicates that the graft copolymer effectively "shields" the immobilized EY* molecules within its polyampholytic matrix. By providing a protective local microenvironment, the polymer suppresses competitive non-radiative relaxation pathways such as collisional quenching by TEOA or deleterious interactions with MoP aggregates, thereby prolonging the residency time of the excited state and enhancing the overall radiative output.

Decays exhibit bi-phasic behavior and were analysed with a segmented approach: an exponential fit for early times (t < 300 ps, yellow curve) and a power-law fit ($f(x) = Ax^{-b}$) for later times (300 ps < t < 1200 ps, green curve), as single functions fail in this heterogeneous system (Fig. 6b). The adoption of a power-law fit for the later decay regime is necessitated by the structural and kinetic complexity of this multi-component hybrid system. Such non-exponential kinetics are characteristic of distributed relaxation rates in heterogeneous media, likely arising from fractal-like diffusion of charge carriers or restricted molecular mobility within the varying microenvironments of the graft copolymer-MoP domains.[48,49] This power-law tail persists even without polymer, signalling baseline microdomain heterogeneity from MoP and TEOA aggregates. The extension of the EY* excited-state lifetime and the confinement within fractal-like

microdomains suggest that the graft copolymer acts as a molecular scaffold. This scaffold optimizes the spatial arrangement of the photosensitizer and catalyst, facilitating efficient charge transfer while minimizing non-productive recombination, thereby directly accounting for the 177% increase in hydrogen evolution (2.5 *vs.* 0.9 $mmol_{H_2}$ h^{-1} g^{-1}) compared to the copolymer-free system.

To assess the stability of the hybrid graft copolymer component (1 g L^{-1} PDha-*g*-*n*PAA, 0.1 g L^{-1} EY, 0.06 g L^{-1} MoP), samples were recovered after 30 h of photocatalysis by dialysis (3.5 kDa cutoff) and subsequent freeze-drying prior to analysis. Thermogravimetric analysis shows no significant change in the onset or profile of thermal degradation for the hybrid before and after irradiation ((PDha-*g*-*n*PAA)-EY-MoP-Bf *vs.* (PDha-*g*-*n*PAA)-EY-MoP-Af; Fig. 7a), indicating that the organic matrix remains thermally robust under the catalytic conditions. SEC analysis of the recovered hybrid (Fig. 7b, normalized RI response) reveals that the number-average molar mass (M_n = 36.600 g mol^{-1}) remains essentially unchanged compared to the pristine graft copolymer (M_n = 38.500 g mol^{-1}). Interestingly, a low-molecular-weight shoulder observed in the pristine polymer (eluting at higher volumes) is absent in the recovered material. This suggests a preferential removal of shorter oligomeric chains during the centrifugation and recovery of the hybrid graft copolymer. The stability of the principal elution peak position confirms that the high-molecular-weight graft copolymer backbone remains intact and does not undergo detectable degradation under photocatalytic conditions. FTIR spectra of the PDha-*g*-*n*PAA graft copolymer retained its characteristic bands, confirming structural integrity after photocatalysis (Fig. 7c). Key backbone peaks included broad O–H and N–H stretching vibrations around 3200–3500 cm^{-1}, C=O stretching of amide and ester groups at 1650–1700 cm^{-1}, alkyl C–H stretching between 2850 and 2950 cm^{-1}, and N–H bending and C–N stretching modes near 1400–1500 cm^{-1}. Distinct peaks associated with immobilization were observed at 1438 cm^{-1}, corresponding to CH_2/CH_3 bending and symmetric COO^- stretching vibrations; 1489 cm^{-1}, attributed to CH_3 asymmetric bending and aromatic C–C stretching from EY; as well as 2849 cm^{-1} and 2932 cm^{-1} which represent symmetric and asymmetric C–H stretching of alkyl groups. These peaks were absent or weak in the graft copolymer alone, confirming successful immobilization. Molybdenum phosphide (MoP), due to its metallic nature, exhibits weak FTIR activity and contributes minimal direct spectral features. No evidence of chemical degradation or new byproduct formation was detected, supporting the hybrid material's chemical stability during catalysis.

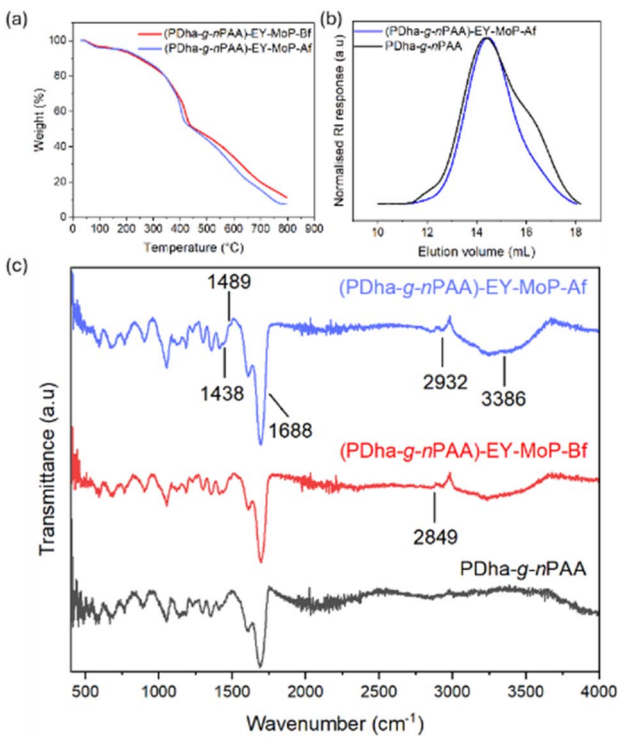

Fig. 7 Thermograms of (PDha-*g*-*n*PAA)-EY-MoP-Bf and (PDha-*g*-*n*PAA)-EY-MoP-Af (a); SEC traces of the graft copolymer (M_n = 38.500 g mol^{-1}) and the hybrid system (PDha-*g*-*n*PAA)-EY-MoP-Af (M_n = 36.600 g mol^{-1}) using PEG calibration in phosphate buffer at pH 11 (baseline-corrected and normalized to the peak maximum to facilitate a qualitative comparison of the elution profiles and molecular weight distributions, (b)); FTIR spectra of PDha-*g*-*n*PAA, (PDha-*g*-*n*PAA)-EY-MoP-Bf, and (PDha-*g*-*n*PAA)-EY-MoP-Af (c).

These results collectively confirm that the graft copolymer remains structurally stable under photocatalytic conditions, supporting its suitability as a robust matrix for hydrogen production. Compared to earlier studies where EY was covalently grafted to molybdenum-based clusters or electrostatically adsorbed onto Mo-based cocatalysts,[23,50,51] this work demonstrates that PDha-based polyampholyte graft copolymers are a simple, tunable, and effective method to achieve stable EY sensitization on MoP with enhanced activity and stability for light-driven H_2 evolution.

Conclusion

We report the successful use of a tailor-made polyampholyte graft copolymer for immobilization of MoP nanoparticles as catalyst and EY as photosensitizer. The results reveal that this is a straightforward approach for the preparation of a versatile and tunable soft matter matrix that can effectively co-integrate various molecular components relevant for light-driven catalysis. The graft copolymer functions as a multifunctional scaffold that provides colloidal stability while preserving a highly concentrated local environment of catalytic and photosensitizing moieties. Comparison with polymer-free reference systems demonstrates that this matrix-mediated stabilization is critical for suppressing MoP aggregation and for promoting efficient charge and mass transport pathways, thereby enabling enhanced hydrogen evolution performance. Light-driven catalytic activity for hydrogen production reached 2.5 $mmol_{H_2}$ h^{-1} $g_{MoP}{}^{-1}$ after the graft copolymer was introduced. Therefore, this strategy indicates that polyampholyte graft copolymers can be used to improve and regulate different molecular catalytic systems by immobilizing metallic nanoparticles. This scheme in our opinion paves the way for systems for other combinations of molecular catalysts, dyes, or semiconducting sensitizers.

Conflicts of interest

The authors declare no conflicts of interest.

Data availability

The data supporting this article have been included as part of the supplementary information (SI). The individual raw data sets are available upon request from the authors. Supplementary information: experimental details and procedures, SEC data (Fig. S1), NMR spectra of graft copolymers (Fig. S2 and S3), Raman spectra (Fig. S4), thermograms of MoP (Fig. S5), XPS spectra (Fig. S6 and S7). See DOI: https://doi.org/10.1039/d6ta00720a.

Acknowledgements

This project was supported by the Deutsche Forschungsgemeinschaft within the Sonderforschungsbereich SFB/TRR 234 "Catalight" (project ID: 364549901, projects B03, B10, B11 and Z02). We thank Laura Calderón Rodríguez, Nigar Aslanova, Grit Festag, Andreas Stihl, Sreevalsan Achikkulathu, Kai Hetze and Akuila Edwards for their assistance with TGA, SEC, cryo-TEM, XRD, and Raman spectroscopy measurements, as well as the NMR department at Friedrich-Schiller University Jena for their support. Falko Langenhorst acknowledges granting of the TEM facilities by the DFG (German Research Foundation, LA830/14-1).

References

1 D. Monga, *et al.*, Recent advances in various processes for clean and sustainable hydrogen production, *Nano-Struct. Nano-Objects*, 2023, **33**, 100948.
2 A. S. Morshedy, *et al.*, A review on heterogeneous photocatalytic materials: mechanism, perspectives, and environmental and energy sustainability applications, *Inorg. Chem. Commun.*, 2024, 112307.
3 T. P. Yoon, M. A. Ischay and J. Du, Visible light photocatalysis as a greener approach to photochemical synthesis, *Nat. Chem.*, 2010, **2**(7), 527–532.
4 D. M. Schultz and T. P. Yoon, Solar synthesis: prospects in visible light photocatalysis, *Science*, 2014, **343**(6174), 1239176.
5 P. Wang, *et al.*, A broadband and strong visible-light-absorbing photosensitizer boosts hydrogen evolution, *Nat. Commun.*, 2019, **10**(1), 3155.
6 H. Xing, *et al.*, Effect of Pt cocatalyst on visible light driven hydrogen evolution of anthracene-based zirconium metal-organic framework, *Appl. Surf. Sci.*, 2020, **532**, 147000.
7 L. Li, *et al.*, Band-gap engineering of layered covalent organic frameworks *via* controllable exfoliation for enhanced visible-light-driven hydrogen evolution, *Int. J. Hydrogen Energy*, 2020, **45**(4), 2689–2698.
8 X. Liu, *et al.*, Visible-light-driven hydrogen evolution with polyoxometalate as electron relay, *J. Photon. Energy*, 2016, **6**(4), 046501.
9 L. Pei, *et al.*, A novel visible-light-responsive semiconductor ScTaO4− xNx for photocatalytic oxygen and hydrogen evolution reactions, *ChemCatChem*, 2021, **13**(1), 180–184.
10 Y. Liu, *et al.*, Metal–organic frameworks containing xanthene dyes for photocatalytic applications, *Dalton Trans.*, 2020, **49**(48), 17520–17526.
11 Y. Shi and B. Zhang, Recent advances in transition metal phosphide nanomaterials: synthesis and applications in hydrogen evolution reaction, *Chem. Soc. Rev.*, 2016, **45**(6), 1529–1541.
12 E. Farahi and N. Memarian, Nanostructured nickel phosphide as an efficient photocatalyst: effect of phase on physical properties and dye degradation, *Chem. Phys. Lett.*, 2019, **730**, 478–484.
13 S. Cao, *et al.*, Cobalt phosphide as a highly active non-precious metal cocatalyst for photocatalytic hydrogen production under visible light irradiation, *J. Mater. Chem. A*, 2015, **3**(11), 6096–6101.
14 G. Li, *et al.*, Carbon-tailored semimetal MoP as an efficient hydrogen evolution electrocatalyst in both alkaline and acid media, *Adv. Energy Mater.*, 2018, **8**(24), 1801258.
15 Y. Gao, *et al.*, Simple synthesis of two-dimensional MoP2 nanosheets for efficient electrocatalytic hydrogen evolution, *Electrochem. Commun.*, 2018, **97**, 27–31.
16 O. O. Dada, *et al.*, Theoretical insights of electrocatalytic hydrogen evolution on MoP nanocrystal, *Int. J. Hydrogen Energy*, 2023, **48**(89), 34634–34648.
17 X. Chen, *et al.*, Molybdenum phosphide: a new highly efficient catalyst for the electrochemical hydrogen evolution reaction, *Chem. Commun.*, 2014, **50**(79), 11683–11685.
18 S. Yin, *et al.*, A highly efficient noble metal free photocatalytic hydrogen evolution system containing MoP and CdS quantum dots, *Nanoscale*, 2016, **8**(30), 14438–14447.
19 L. Zhang, *et al.*, Nanohybrid of carbon quantum dots/molybdenum phosphide nanoparticle for efficient electrochemical hydrogen evolution in alkaline medium, *ACS Appl. Mater. Interfaces*, 2018, **10**(11), 9460–9467.
20 C. Cheng, *et al.*, Facile preparation of nanosized MoP as cocatalyst coupled with g-C3N4 by surface bonding state for enhanced photocatalytic hydrogen production, *Appl. Catal., B*, 2020, **265**, 118620.
21 J.-y. Tang, *et al.*, Noble-metal-free molybdenum phosphide co-catalyst loaded graphitic carbon nitride for efficient photocatalysis under simulated irradiation, *J. Catal.*, 2019, **370**, 79–87.
22 W. Liu, *et al.*, Porous MoP network structure as co-catalyst for H2 evolution over g-C3N4 nanosheets, *Appl. Surf. Sci.*, 2018, **462**, 822–830.
23 J. Xu, *et al.*, Optimal preparation of molybdenum phosphide cocatalyst for efficient dye-sensitized photocatalytic hydrogen evolution, *Int. J. Hydrogen Energy*, 2022, **47**(6), 3814–3823.
24 J. J. Leung, *et al.*, Photoelectrocatalytic H 2 evolution in water with molecular catalysts immobilised on p-Si *via*

a stabilising mesoporous TiO 2 interlayer, *Chem. Sci.*, 2017, **8**(7), 5172–5180.
25 T. Yang, *et al.*, Immobilization of Pt nanoparticles in carbon nanofibers: bifunctional catalyst for hydrogen evolution and electrochemical sensor, *Electrochim. Acta*, 2015, **167**, 48–54.
26 N. M. Muresan, *et al.*, Immobilization of a molecular cobaloxime catalyst for hydrogen evolution on a mesoporous metal oxide electrode, *Angew. Chem., Int. Ed.*, 2012, **51**(51), 12749.
27 A. Nabiyan, *et al.*, Polyampholytic Graft Copolymers as Matrix for TiO2/Eosin Y/[Mo3S13] 2− Hybrid Materials and Light-Driven Catalysis, *Chem. - Eur. J.*, 2021, **27**(68), 16924–16929.
28 D. Costabel, *et al.*, Diiodo-BODIPY Sensitizing of the [Mo3S13] 2–Cluster for Noble-Metal-Free Visible-Light-Driven Hydrogen Evolution within a Polyampholytic Matrix, *ACS Appl. Mater. Interfaces*, 2023, **15**(17), 20833–20842.
29 U. Günther, *et al.*, Polyelectrolytes with tunable charge based on polydehydroalanine: synthesis and solution properties, *Macromol. Chem. Phys.*, 2013, **214**(19), 2202–2212.
30 J. Max, *et al.*, Polyampholytic Poly (dehydroalanine) Graft Copolymers as Smart Templates for pH-Controlled Formation of Alloy Nanoparticles, *Macromolecules*, 2020, **53**(11), 4511–4523.
31 J. Max, *et al.*, Polyampholytic graft copolymers based on polydehydroalanine (PDha)–synthesis, solution behavior and application as dispersants for carbon nanotubes, *Polym. Chem.*, 2019, **10**(23), 3006–3019.
32 J. B. Max, *et al.*, Triple-Responsive Polyampholytic Graft Copolymers as Smart Sensors with Varying Output, *Macromol. Rapid Commun.*, 2021, **42**(7), 2000671.
33 I. Gitsov and F. E. Johnson, Synthesis and hydrolytic stability of poly (oxyethylene-H-phosphonate) s, *J. Polym. Sci., Part A: Polym. Chem.*, 2008, **46**(12), 4130–4139.
34 Y. J. Yin, *et al.*, A study on biomineralization behavior of N-methylene phosphochitosan scaffolds, *Macromol. Biosci.*, 2004, **4**(10), 971–977.
35 N. Hu, *et al.*, Acrylamide monomers and polymers that contain phosphonate ions, *Polymer*, 2015, **65**, 124–133.
36 S. Harrisson, P. Couvreur and J. Nicolas, Simple and efficient copper metal-mediated synthesis of alkoxyamine initiators, *Polym. Chem.*, 2011, **2**(8), 1859–1865.
37 S. Rundqvist and T. Lundström, *X-Ray Studies of Molybdenum and Tungsten Phosphides*, 1962.
38 Z. Pu, *et al.*, Semimetallic MoP 2: an active and stable hydrogen evolution electrocatalyst over the whole pH range, *Nanoscale*, 2016, **8**(16), 8500–8504.
39 T. Wu, *et al.*, Three-dimensional porous structural MoP2 nanoparticles as a novel and superior catalyst for electrochemical hydrogen evolution, *J. Power Sources*, 2016, **328**, 551–557.
40 S. Knapp, *et al.*, Thermogravimetric analysis of molybdenum oxide (MoO3) decomposition, in *47th International Annual Conference of ICT*, 2016.
41 Y. He, *et al.*, Polymer degradation: Category, mechanism and development prospect, in *E3S Web of Conferences*, EDP Sciences, 2021.
42 S. E. Kudaibergenov, Catalytic Properties of Polyampholytes, Polyampholyte-Metal Complexes, Polyampholyte-Metal Nanoparticles and Polyampholyte-Enzyme Conjugates: a Mini-Review, *Eurasian J. Chem.*, 2024, **29**(3), 42–54.
43 D. Kowalczyk, *et al.*, Making Photocatalysis Comparable Using a Modular and Characterized Open-Source Photoreactor, *ChemPhotoChem*, 2022, **6**(7), e202200044.
44 R. Abe, *et al.*, Steady hydrogen evolution from water on Eosin Y-fixed TiO2 photocatalyst using a silane-coupling reagent under visible light irradiation, *J. Photochem. Photobiol., A*, 2000, **137**(1), 63–69.
45 C. Li, *et al.*, Covalent organic frameworks with high quantum efficiency in sacrificial photocatalytic hydrogen evolution, *Nat. Commun.*, 2022, **13**(1), 2357.
46 A. Lewandowska-Andrałojć, *et al.*, How Eosin Y/graphene oxide-based materials can improve efficiency of light-driven hydrogen generation: Mechanistic aspects, *J. Phys. Chem. C*, 2020, **124**(5), 2747–2755.
47 F. Herbrik, *et al.*, Eosin Y: homogeneous photocatalytic in-flow reactions and solid-supported catalysts for in-batch synthetic transformations, *Appl. Sci.*, 2020, **10**(16), 5596.
48 C. Günnemann, *et al.*, Charge carriers in commercial photocatalysts: fractal kinetics and effect of "inert" additives, *Top. Catal.*, 2021, **64**(13), 737–747.
49 D. S. Banks, *et al.*, Characterizing anomalous diffusion in crowded polymer solutions and gels over five decades in time with variable-lengthscale fluorescence correlation spectroscopy, *Soft Matter*, 2016, **12**(18), 4190–4203.
50 X. Liu, *et al.*, Graphene decorated MoS 2 for eosin Y-sensitized hydrogen evolution from water under visible light, *RSC Adv.*, 2017, **7**(74), 46738–46744.
51 A. Denikaev, *et al.*, Covalent Grafting of Eosin Y to the Giant Keplerate {Mo132} through an Organosilicon Linker in Homogeneous Regime, *Inorganics*, 2023, **11**(6), 239.

